



**HAL**  
open science

# Electrochemical Protocols to Assess the Effects of Dissolved Transition Metal in Graphite/LiNiO<sub>2</sub> Cells Performance

Valentin Meunier, Matheus Leal de Souza, Mathieu Morcrette, Alexis Grimaud

► **To cite this version:**

Valentin Meunier, Matheus Leal de Souza, Mathieu Morcrette, Alexis Grimaud. Electrochemical Protocols to Assess the Effects of Dissolved Transition Metal in Graphite/LiNiO<sub>2</sub> Cells Performance. Journal of The Electrochemical Society, 2022, 169 (7), 10.1149/1945-7111/ac7e7a . hal-03740625

**HAL Id: hal-03740625**

**<https://u-picardie.hal.science/hal-03740625>**

Submitted on 8 Jun 2023

**HAL** is a multi-disciplinary open access archive for the deposit and dissemination of scientific research documents, whether they are published or not. The documents may come from teaching and research institutions in France or abroad, or from public or private research centers.

L'archive ouverte pluridisciplinaire **HAL**, est destinée au dépôt et à la diffusion de documents scientifiques de niveau recherche, publiés ou non, émanant des établissements d'enseignement et de recherche français ou étrangers, des laboratoires publics ou privés.

**OPEN ACCESS**

# Electrochemical Protocols to Assess the Effects of Dissolved Transition Metal in Graphite/LiNiO<sub>2</sub> Cells Performance

To cite this article: Valentin Meunier *et al* 2022 *J. Electrochem. Soc.* **169** 070506

View the [article online](#) for updates and enhancements.

## You may also like

- [Lattice location of implanted transition metals in 3C-SiC](#)  
A R G Costa, U Wahl, J G Correia et al.
- [Electronic structure evolution of the transition metals substituted tetragonal graphene: a first-principles investigations](#)  
Surasree Sadhukhan and Sudipta Kanungo
- [Interactions of toroidally coupled tearing modes in the KSTAR tokamak](#)  
Gnan Kim, Gunsu S Yun, Minho Woo et al.



# Electrochemical Protocols to Assess the Effects of Dissolved Transition Metal in Graphite/LiNiO<sub>2</sub> Cells Performance

Valentin Meunier,<sup>1,2</sup>  Matheus Leal De Souza,<sup>2,3</sup>  Mathieu Morcrette,<sup>2,3</sup> and Alexis Grimaud<sup>1,2,z</sup> 

<sup>1</sup>Chimie du Solide et de l'Energie (CSE), Collège de France, UMR 8260, 75231 Paris Cedex 05, France

<sup>2</sup>Réseau sur le Stockage Electrochimique de l'Energie (RS2E), CNRS FR 3459, 80039 Amiens Cedex, France

<sup>3</sup>Laboratoire de Réactivité et Chimie des Solides (LRCS), UMR CNRS 7314, Université de Picardie Jules Verne, HUB de l'Energie, 80039 Amiens, France

The deployment of energy dense positive electrode materials such as Ni-rich NMC (LiNi<sub>x</sub>Mn<sub>y</sub>Co<sub>z</sub>O<sub>2</sub> with 0 < x, y, z < 1 and x + y + z = 1) for Li-ion batteries is plagued by numerous interfacial limitations. Among them, dissolution of transition metals (TMs) was shown to trigger deleterious growth of solid electrolyte interphase (SEI) and/or lithium plating at the anode. Although numerous post-mortem analysis and cycling data showed a causal relationship between TMs deposition and capacity fading, quantifying and discriminating the major source of degradation proves tedious. Herein, using graphite/LiNiO<sub>2</sub> chemistry, we quantitatively demonstrate that TMs in solution permeate inside the SEI to be reduced, which precipitates cell aging following a loss of lithium inventory at the anode. This loss induces a change in intercalation staging at the graphite anode, allowing the recovery of LiNiO<sub>2</sub> intercalation plateau at high potential, thus leading to a “S”-shape evolution of capacity as function of cycling. Furthermore, aging study in temperature show that TMs do not favor lithium plating but rather destabilize the SEI, especially at high temperature. Beyond the sole understanding of the graphite/LiNiO<sub>2</sub> chemistry, this work offers practical routes towards evaluating LIBs degradations using electrochemical diagnosis methods.

© 2022 The Author(s). Published on behalf of The Electrochemical Society by IOP Publishing Limited. This is an open access article distributed under the terms of the Creative Commons Attribution 4.0 License (CC BY, <http://creativecommons.org/licenses/by/4.0/>), which permits unrestricted reuse of the work in any medium, provided the original work is properly cited. [DOI: 10.1149/1945-7111/ac7e7a]



Manuscript submitted April 15, 2022; revised manuscript received June 21, 2022. Published July 13, 2022.

Supplementary material for this article is available [online](#)

Li-ion batteries (LIB) became an integral component of our everyday life with a wide variety of applications ranging from portable electronics to reshaping today's mobility with the advent of electrical vehicles.<sup>1,2</sup> To improve the performance of LIBs, the deployment of the so-called NMC family (LiNi<sub>x</sub>Mn<sub>y</sub>Co<sub>z</sub>O<sub>2</sub> with 0 < x, y, z < 1 and x + y + z = 1) as positive electrode is now eagerly pursued.<sup>3–5</sup> More specifically, due to restrictions regarding the use of cobalt as well as their enhanced capacity, efforts have been placed in increasing the nickel content and develop Ni-rich phases (x ≥ 0.8). However, Ni-rich compounds suffer from poorer stability, either thermal or chemical, upon cycling, in particular at voltages above 4.2 V.<sup>6</sup> To explain the latter, numerous mechanisms have been described such as particles cracking,<sup>7–9</sup> phase transformation,<sup>10–12</sup> electrolyte oxidation<sup>13,14</sup> or dissolution of transition metals (TMs).<sup>15–18</sup> Although dissolution of TMs was found not to exceed 1% of the total weight of TMs in positive electrode at moderate cycling conditions,<sup>19</sup> this phenomenon has long being discussed to lead to a large portion of the capacity fading observed for Ni-rich compounds, as TMs migrate and deposit on the negative electrode.<sup>15–23</sup> Hence, TMs were proposed to cause a multitude of side reactions, such as catalyzing the SEI formation<sup>24</sup> and leading to the decomposition of solvent- or salt-derived species to a more reduced state.<sup>21,25,26</sup> These TM-induced side reactions were claimed to be associated with a continuous lithium trap into the solid electrolyte interphase (SEI)<sup>17,25</sup> and a raise of cell impedance.<sup>22,24,27</sup> In addition to catalyzing the SEI growth, Klein et al. proposed that transition metal deposition at the anode induces the formation of lithium dendrites, leading to capacity roll-over or, in worst case, to local short-circuits.<sup>28–30</sup> Thus, from the incorporation of TMs into the SEI (which was proposed to follow an ion-exchange mechanism between Li<sup>+</sup> and TM<sup>n+</sup><sup>22,31</sup>) to their interactions and their exact role in capacity fading, the extent to which the release of TMs destabilizes cycling behavior is so far empirically known but not quantitatively understood despite being widely studied.

Post mortem characterization methods such as scanning electron microscopy (SEM),<sup>15,24</sup> X-ray photoelectron spectroscopy (XPS)<sup>24,32,33</sup>

or X-ray absorption spectroscopy (XAS)<sup>17,25,31,34,35</sup> have been employed to comprehend TMs side effects at the negative electrode. In comparison, thorough and quantitative electrochemical investigations regarding lithium loss associated with catalysis of the SEI growth, loss of cathode active materials, or plating phenomenon all associated with TM dissolution and shuttling are rather scarce. Indeed, although these techniques offer diagnosis methods that do not require cell opening, which often induces short circuits or exposure to air, performing such analysis in a quantitative manner requires the use of appropriate cycling methods, such as described elsewhere.<sup>36–41</sup> Gilbert et al.<sup>17</sup> have implemented such advanced electrochemical procedures and demonstrated a causal relationship between TM amounts on graphite electrode and lithium losses. However, neither the effect of TM nature nor the possibility of lithium plating was discussed in this study.

In this work, LiNiO<sub>2</sub> (LNO) was studied as high energy and cobalt-free positive material to investigate damaging effect of TMs deposition on graphite electrode. Using adapted aging procedures and advanced electrochemical analysis, we introduce and discuss the implementation of a complete methodology for assessing the effect of TMs on lithium plating and SEI growth. As well, we demonstrate that once dissolved, TMs undoubtedly incorporate into the SEI and disrupt its stability, in particular at high temperatures, this effect being predominant when compared to catalyzing lithium plating.

## Experimental

**Electrode manufacturing.**—Graphite electrodes were made of 93.2%<sub>wt</sub> of active material (graphite GHDR 10–93, Imerys), 3%<sub>wt</sub> carbon black (Super C45, Timcal) and a blend of 2%<sub>wt</sub> carboxymethylcellulose (CMC), 1%<sub>wt</sub> styrene-butadiene rubber (SBR) and 0.8%<sub>wt</sub> surfactant (TritonX). Solvent, osmosed water produced with a Merck Millipore (MilliQ), was added until obtaining the final dry mass ratio (total powder mass / (solvent + powder mass)) of 37%<sub>wt</sub>. Positive electrodes consisted in 92%<sub>wt</sub> of LiNiO<sub>2</sub> (LNO, BASF, Germany), 4%<sub>wt</sub> polyvinylidene fluoride (PVDF) binder and 4%<sub>wt</sub> carbon black (Super C45, Timcal); N-methyl-2-pyrrolidone (NMP, DoDoChem, 99.9%) was added until the final dry mass ratio was set to 25%<sub>wt</sub>. Both inks were respectively cast on 20 μm thick copper and aluminum current collectors and then calendered to reduce the

<sup>z</sup>E-mail: alexis.grimaud@college-de-france.fr

porosity down to ca. 30%. The obtained final active material loadings are 4.2 mg.cm<sup>-2</sup> for graphite and 5.6 mg.cm<sup>-2</sup> for LNO.

**Coin cell assembly.**—All coin cells were assembled in argon filled glove box using 2032-type casing, 1.23 mm thick wave springs and a set of 0.5 and 1 mm 316-stainless steel spacers (AOT Battery, China). Electrodes were punched into circular disks of Ø14 mm (positive) and Ø15 mm (negative) and dried overnight at 80 °C under reduced pressure. Negative capacity was 1.5-fold oversized compared to the positive one, giving a balancing N/P ratio = 1.5. Experimental capacities were used considering that no additional capacity is measured above 4.2 V in graphite/LNO cells. Polypropylene films (Celgard 2500) were punched and dried at 55 °C overnight before use and added as a single layer separator. During assembly, electrodes and separator were soaked with 30 µL of LP57 electrolyte (1 M LiPF<sub>6</sub> in EC:EMC 30:70<sub>wt</sub>—E-lyte, Germany), added in two steps: 15 µL on the anode and the remaining 15 µL on the separator.

**Study of transition metal effects.**—To study the effect of transition metal ions, nickel bis(trifluoromethylsulfonyl)imide Ni(TFSI)<sub>2</sub>, manganese bis(trifluoromethylsulfonyl)imide Mn(TFSI)<sub>2</sub> and cobalt bis(trifluoromethylsulfonyl)imide Co(TFSI)<sub>2</sub> salts (Alfa-Aesar, 97.0 + %) were dissolved in 1.000 mL of LP57 electrolyte. Metal concentrations were set to 665 ppm, corresponding to about 0.5% in weight of the total amount of nickel contained in the positive electrode.

**Electrochemical tests.**—Cells were cycled at 25 °C in controlled temperature chamber (Mettler, Germany) with a BCS-810 potentiostat (BioLogic, France). Before the first charge, cells were rested for 6 h to let the electrolyte fills the electrode/separator porosity and reach thermal equilibrium. Gravimetric capacity based on the LNO active mass is used. Similar currents were applied during charge and discharge, referred to as C-rates and D-rate, respectively. Cycling was performed from 2.5 V to 4.2, 4.5 or 4.8 V with C-rates defined from theoretical capacity of LNO ( $Q_{th} = 275 \text{ mAh.g}^{-1}$ ). After a formation step consisting in two C/20–D/20 cycles, an “aging” period was carried out at C/2–D/2 current with a constant voltage step at the end of each charge until current is measured below C/20. Every 10-cycles, a so-called “control cycle” was implemented to check the cell performance at low current (C/20–D/20) and perform the slippage analysis (detailed below).

**Aging in temperatures.**—All cells were first preconditioned using two cycles at C/20–D/20 at 25 °C in a controlled temperature chamber (Mettler, Germany). Afterwards, independent cells were aged at the different temperatures of interest (from 15 °C to 55 °C). The cycling procedure started with a 6 h open circuit voltage (OCV) rest to reach the thermal equilibrium followed by an aging control procedure consisting of the repetition of a slow cycle (C/20–D/20) alternated with 10-cycles C/2–D/2, with a CV step at the end of charge  $i < C/20$ . Degradation rates are subsequently defined as the difference of discharge capacity between two control cycles, normalized by cycling time, working electrode surface area and mass. For lithium plating study, the aging current was raised up to 3 C (instead of C/2) and capacity balancing reduced to 1.3 (1.5 previously). For each tested condition, cells were duplicated.

**Cyclic voltammetry (CV).**—Cyclic voltammograms were recorded using 2032-coin cells in a two-electrodes configuration. Half-charged LiFePO<sub>4</sub> was used as reference/counter electrode and polished copper foil as working electrode. Potential was scanned at 0.1 mV.s<sup>-1</sup> between OCV (3.45 V vs Li<sup>+</sup>/Li) and 0.005 V vs Li<sup>+</sup>/Li with LP57 or LP57 + 665 ppm Ni<sup>2+</sup>. For the tests conducted with SEI formed during a separate step, LP57 was first reduced on copper foil during three consecutive scans at 0.1 mV.s<sup>-1</sup> between 3.45 V and 0.005 V vs Li<sup>+</sup>/Li. Afterwards, foil was recovered and reused in a new coin cell setup with nickel-contaminated electrolyte (665 ppm). Same scanning conditions as described above were then used.

**Inductively coupled plasma mass spectroscopy (ICP-MS).**—Nickel leaching was quantified from graphite electrodes using inductively coupled plasma mass spectroscopy (ICP-MS, Nexion 2000, Perkin Elmer). Beforehand, cells were cycled as follow: one formation cycle (C/20–D/20), 10-aging cycles (CCCV, C/2,  $i < C/20$ –D/2) and one and a half cycle (C/20–D/20–C/20) with a 4.2, 4.5 or 4.8 V cutoff voltage. Cells were stopped in charged state i.e. LiNiO<sub>2</sub> in delithiated state and graphite electrodes in lithiated state. Cells were then de-crimped in argon-filled glove box to recover negative electrodes and immediately rinsed front and back with c.a. 5 mL in total of dimethyl carbonate (DMC) to remove nickel-contaminated electrolyte on graphite surface. Wash time and solvent volume were minimized to alleviate the risks of SEI dissolution and any loss of nickel. Graphite electrodes were subsequently dissolved in 10 mL of 2%<sub>wt</sub> nitric acid (Suprapur, 65% HNO<sub>3</sub>, Merck) and solutions sonicated and rested overnight. Solutions were filtered with polypropylene 0.2 µm filters (VWR) and diluted with 2%<sub>wt</sub> nitric acid solution until final nickel concentrations between 1 ppb and 1 ppm were obtained. Dilution step was duplicated to obtain experimental error bars, as reported on the figures. The calibration was obtained from nine diluted nickel standard solutions (TraceCERT, 1 mg.L<sup>-1</sup> Ni in nitric acid, Sigma-Aldrich).

**Slippage analysis.**—Slippage analysis was performed by fitting the differential voltage (dV/dQ vs Q) of discharge curves obtained during the control cycles, (0th, 2nd, 4th and 6th control cycles). This method requires recording cycles at low current to recover accessible capacity and limit kinetic artifacts during phase transitions of materials i.e. to work in quasi-equilibrium conditions. To limit the noisiness of the dV/dQ curves associated with the slow discharge rates, the number of points was reduced down to 100 points with linear interpolation. Graphite and LiNiO<sub>2</sub> half-cell reference curves were measured at C/20–D/20 at the same temperature as that of the full cell, and were used to rebuild a dV/dQ model of the full cell following the equation:  $(dV/dQ)_{cell} = (dV/dQ)_{pos.ref.} - (dV/dQ)_{neg.ref.}$ . The model is a function of active material masses and capacity slippages associated with cell degradations, which were latter adjusted to fit the measured dV/dQ of control cycle. Fitting were performed using the VAWQuum v1.2 freeware.

## Results and Discussion

To study the degradation phenomena associated with increased cut-off potential, graphite/LNO cells were cycled at 25 °C from 2.5 V to an upper voltage cutoff of 4.2, 4.5 or 4.8 V. After two initial formation cycles at a current of C/20–D/20, a cycling protocol described in Fig. 1a alternating between *Aging* (CCCV, C/2  $i < C/20$ –D/2) and *Control cycles* (C/20–D/20) was used for periodically diagnose cell performance. Since the high voltage intercalation plateau for LNO occurs at 4.15 V in graphite/LNO full cell, corresponding to 4.2 vs Li<sup>+</sup>/Li (Figure S1, available online at [stacks.iop.org/JES/169/070506/mmedia](https://stacks.iop.org/JES/169/070506/mmedia)), similar capacities were observed for 4.2, 4.5 and 4.8 V cutoff voltage (Fig. 1b, upper panel). However, for 4.8 V, extra capacity was initially spotted up to the 30th cycle. This extra capacity is associated with parasitic reaction, most likely due to electrolyte oxidation at the positive electrode, which origins will be discussed below. Subsequently, increasing the cutoff voltage above 4.5 V significantly affects the cell performance, with capacity losses of 25% (4.5 V) and 55% (4.8 V) recorded at the 6th control cycle compared to 21% at 4.2 V. These degraded performance were confirmed by observing the lower coulombic efficiencies (CEs) recorded at greater cutoff potential (Fig. 1b, bottom panel).

Our attention then turned to the effect of cycling protocol, and especially the use of a slow control cycle every 10 cycles, on the cell performance. When using cutoff potential of 4.2 and 4.5 V, CEs greater than 100% were recorded for each control cycle throughout the cycling, revealing an artefact related to the testing protocol when changing the current density (Fig. 1b, lower panel). Indeed, during

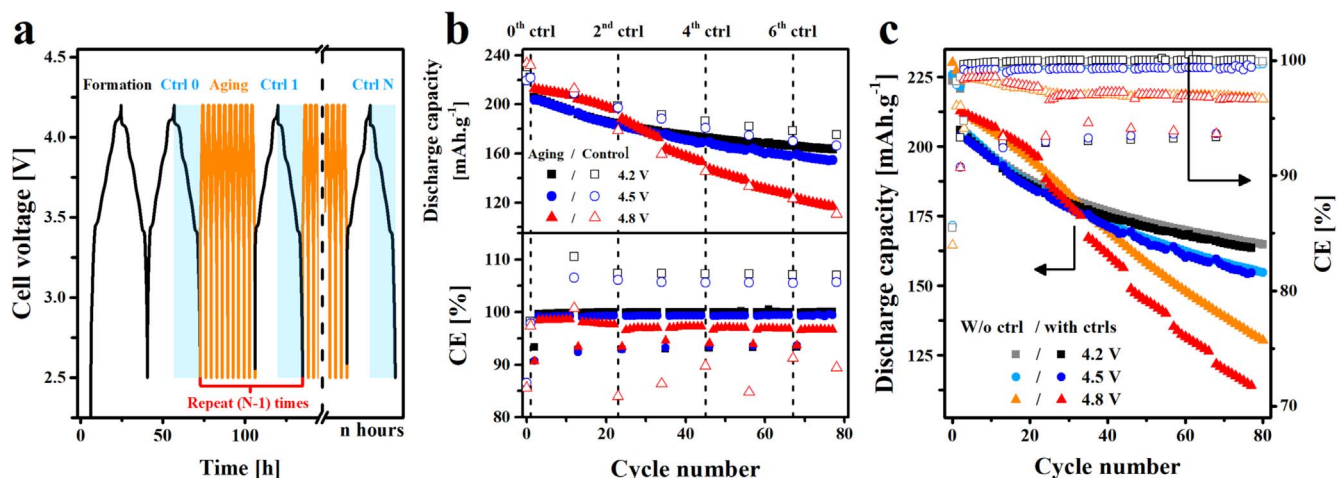


**Figure 1.** Evaluation of graphite/LNO performance using aging protocols. (a) Cycling protocol employed to periodically diagnose cell performance of graphite/LNO cells. Aging consists in ten consecutive C/2–D/2 cycles with a constant voltage (CV) step at the end of each charge until current is lower than C/20. Afterwards, control cycle is performed at C/20–D/20 to assess cell performance and perform dV/dQ analysis on discharge (shaded blue part). (b) Capacity retention and coulombic efficiency plot for cells measured at different voltage cutoffs (4.2, 4.5 and 4.8 V). (c) Capacity retention and coulombic efficiencies measured using continuous cycling procedure when compared to the aging protocol described in panel a. All capacities are normalized by LNO active material weight.

the last discharge of the aging step performed at D/2, LNO is not fully relithiated, thus artificially leading to a lower charge capacity during the next charge at C/20. During the following aging cycle at C/2, CEs close to 90% are recorded. This effect originates from the previous D/20 discharge during which more lithium is intercalated in the LNO electrode, which allows to recover additional capacity during the subsequent C/2 charge. Eventually, this artefact is due to different intercalation degrees reached as function of C-rate and does not originate from degradations such as electrolyte oxidation. A second artefact was observed when using this protocol: a lower capacity retention compared to aging cycles carried out without control cycles at low C/rate (Fig. 1c, grey, light blue and orange dots). This capacity loss is observed at high voltage, i.e. when using a 4.8 V cutoff voltage, indicating that low current densities favor parasitic reactions associated with electrolyte oxidation above 4.5 V, hence degrading the full cell performance over time. In addition, at 4.8 V, a small initial capacity drop is observed at the beginning of the 10-aging cycles period following the control cycle. This capacity drop is more pronounced at high voltage, giving rise to a stair shape-like capacity retention curve (Fig. 1c). In definitive, although the cycling procedure adopted in this study is not neutral regarding cell performances, degradation mainly occur from the use of high cutoff voltages (i.e. 4.8 V), reinforcing our will to understand the associated side effects.

The effect of cutoff voltage on cell performance was further studied by comparing the cumulated capacities recorded for the cells (Fig. 2a). From one cycle to the next, the cells experience a shift of discharge capacity endpoints ( $Q_d$ ) towards greater capacities, this event being accentuated with increased cutoff voltage. Lithium loss during the SEI build-up or loss of active mass from the electrodes can both explain this shift, but these two effects cannot be distinguished without further analysis. For a cutoff voltage set at 4.8 V, not only  $Q_d$  but also the charge capacity endpoint ( $Q_c$ ) shift, following an extra oxidation reaction occurring at the positive electrode. Since the high voltage (de)intercalation plateau of LNO occurs at 4.15 V vs graphite, oxidation thus originates from parasitic reactions such as electrolyte oxidation, inducing additional lithium intercalation at the negative electrode.<sup>42</sup> The greater lithiation degree of graphite thus compensates in part the lithium losses associated to the SEI formation, explaining the initial greater discharge capacities observed in Figs. 1b and 1c when using a 4.8 V cutoff potential. Despite this effect, the shift of discharge endpoints remains greater

for 4.8 V cutoff potential (Fig. S2), inducing a continuous shrinkage of cell capacity window (defined as  $Q_c-Q_d$ ), i.e. a loss of cell capacity. In other words, the oxidation process at 4.8 V does not provide sufficient extra capacity to avoid capacity shrinkage, leading to a continuous loss of capacity. Ultimately, the shift in endpoint capacities is due to cell degradations from both electrodes, either in the form of loss of lithium inventory (LLI) through various side reactions or as loss of active material (LAM) through particle cracks or loss of electronic contacts. From the raw electrochemical curves  $V = f(Q)$  or simple performance indicators such as the evolution of capacities or CE vs cycle number, effects related to LLI and LAM cannot be disentangled. However, with further data processing, these crucial information are accessible, as described below.

The nature and the origin of the degradation phenomena can be distinguished by fitting, using references curves for  $\text{LiNiO}_2$  & graphite vs  $\text{Li}^+/\text{Li}$ , the derivative dV/dQ vs Q curves obtained from discharge curves recorded during the control cycles (fits are provided figure S3 for control 0).<sup>36,40</sup> Using a relative capacity scale (Fig. 2b), degradation associated with the negative electrode are visible from a left-shift of the  $\text{LiNiO}_2$  capacity curve (referred to as negative slippage). Indeed, following degradations at the anode such as LLI occurring during the SEI formation, the positive material is not fully relithiated at the end of discharge. In a similar manner, degradations at the positive electrode can be seen by a left-shift of the graphite capacity curve (referred to as positive slippage), revealing that some amount of lithium remains in graphite at the end of discharge following an extra lithiation resulting from solvent oxidation, as discussed above. Ultimately, oxidation and reduction parasitic events lead to continuous modification of lithiation degrees of respective electrodes over cycling. However, the associated capacity slippages are only visible if degradations occurring at one electrode prevail over the other. In other words, if both positive and negative parasitic capacities compensate each other, SEI can grow and the solvent oxidize without recording any capacity slippage. Evidently, this holds true if the mass of active materials remains unchanged.

In Fig. 2b, a negative slippage which increases over cycling is observed independently of the cutoff voltage (from light to dark blue). This negative slippage is associated with LLI during the initial SEI growth and its evolution over cycling, i.e. its repairing process. The negative slippage is fairly similar for cutoff voltages of 4.2 and 4.5 V. Furthermore, after the 4th control cycle, slippage directions

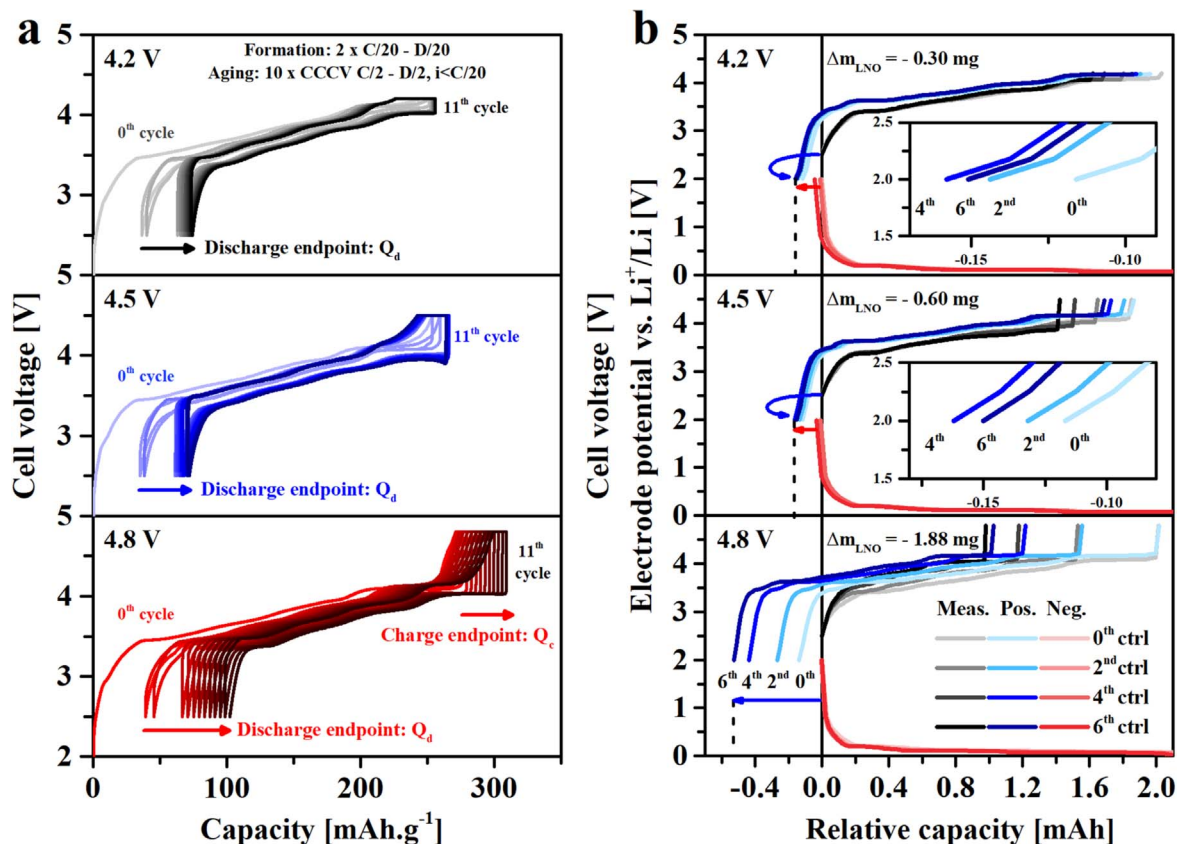


**Figure 2.** Graphite/LNO capacity degradation. (a) Cumulative capacities recorded at 4.2, 4.5 and 4.8 V, with capacity slippage and end of charge ( $Q_c$ ) and discharge ( $Q_d$ ) being indicated. Capacity is normalized by LNO active material weight. (b) Associated dV/dQ analysis showing capacity degradations mainly originating from lithium loss inventory, as indicated by the negative shift of positive electrode curve.

flipped to the right (see insets in Fig. 2b) and the positive slippage is observed to increase simultaneously. This phenomenon indicates a switch in degradation regime where lithium loss at the negative electrode slows down relative to any degradation phenomena occurring at the positive. In other words, from the 40<sup>th</sup> aging cycle, less and less lithium is trapped into the SEI from one cycle to the next, suggesting its stabilization. A loss of positive active material also intensifies this reversal phenomenon, as less intercalation sites are available due to particle cracking while the lithium inventory remains steady (no drastic modification of the dQ/dV curves is visible in figure S4, suggesting that nickel migration toward interlayers is not the major contributor to this phenomenon). As a result, the apparent lithiation degree of LNO re-increased. Still, negative slippage is found dramatically greater, suggesting massive parasitic reactions, consistent with the poorer capacity retention and coulombic efficiency observed in Fig. 1b. Furthermore, the switch in degradation regime is not observed at 4.8 V where negative slippage continuously shifts to the left, indicating that the growth of the SEI and its repair prevails longer. As no positive slippage was observed, parasitic oxidation events occurring during charge at the positive electrode leads to additional lithium cations being inserted into the negative electrode, these cations being utilized during the subsequent discharge when the graphite electrode is found fully delithiated. Hence, as the anodic parasitic reactions almost perfectly compensate for the lithium losses at the negative electrode, the deleterious electrolyte oxidation artificially extends cell performances in early cycles. Nevertheless, caution must be exercised when performing dV/dQ analysis using large cutoff potentials such as 4.8 V or 4.5 V as they can induce gradual changes in the potential curves associated with bulk degradations during H2→H3 phase transition.<sup>43</sup> At 4.2 V, LNO still experiences deleterious phase

transition but structural degradations are not prejudicial for dV/dQ fitting up to the 6<sup>th</sup> control, as show in figure S5, regardless of the electrolyte used.

Degradations related to losses of lithium associated with SEI growth or other parasitic reactions can thus be diagnosed by employing the differential voltage analysis. Furthermore, positive LAM can also be extracted from this analysis. Using 4.2 V cutoff voltage, LAM was found to account for 3.3% of the initial LNO mass at the 6<sup>th</sup> control cycle, while as much as 27.8% LAM was measured at 4.8 V, demonstrating a strong voltage dependency. Particles crack, loss of electric contacts or nickel dissolution can all participate to LAM, but their relative extent cannot be assessed using the dV/dQ analysis. Furthermore, as previously discussed in the literature, dissolved transition metal such as nickel are known to precipitate the cell failure. Our attention therefore turned into quantifying the amount of leached TM to further understand the origin of cell degradations.

To separate TM dissolution from the inherent loss of LNO active material by electrochemical grinding or irreversible structural modifications, the amount of leached nickel was quantified after deposition on graphite electrodes. Cells were thus cycled as follow: one formation cycle (C/20–D/20), 10-aging cycles (CCCV: C/2;  $i < C/20$ –D/2) and one and half cycle (C/20–D/20–C/20) (equivalent to control 0, aging and control 1 in Fig. 1a). Cells were then opened in charged state, rinsed and the amount of nickel quantified by inductively coupled plasma—mass spectrometry (ICP-MS). As shown in Fig. 3a, the amount of nickel found on the surface of graphite electrodes increases nearly exponentially with the cutoff voltage. Hence, at 4.8 V, 0.5%<sub>wt</sub> of the nickel contained in the LNO positive electrode, equivalent to 665 ppm in the electrolyte (30  $\mu$ L), was measured, consistent with previous observations.<sup>17</sup> One must

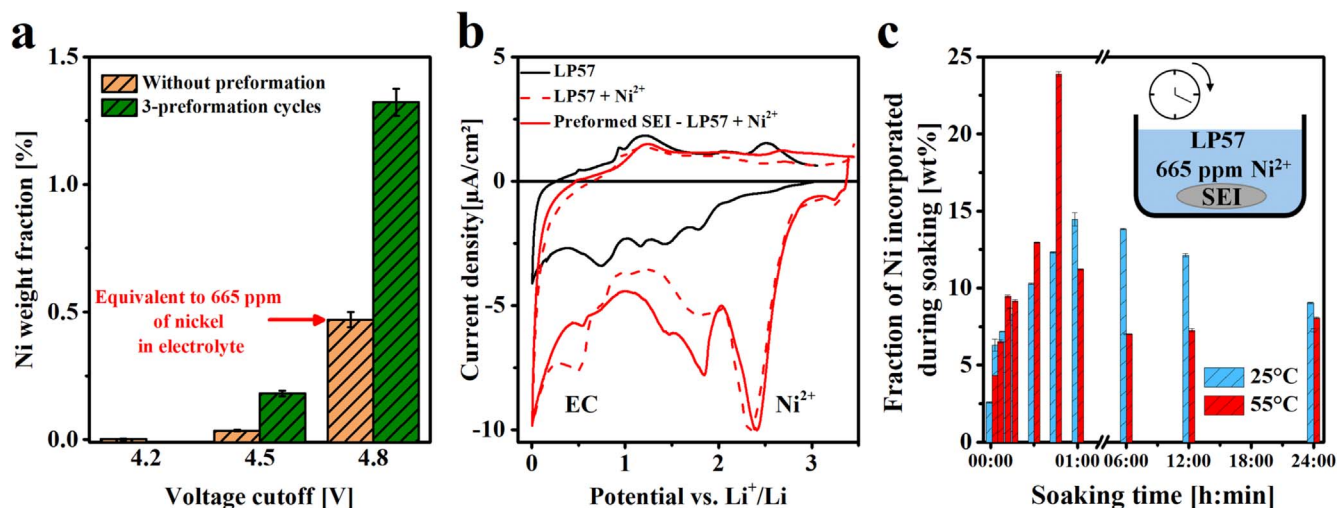


**Figure 3.** Interaction between leached nickel cations and the SEI. (a) Amounts of nickel detected in graphite electrodes SEI (orange) and with SEI formed during longer formation cycles (green, two additional C/20 cycles beforehand) as a function of cutoff voltage. (b) Cyclic voltammograms showing reduction of nickel cations on copper foil for LP57 electrolyte (black), LP57 + 665 ppm Ni<sup>2+</sup> (red dotted line) and LP57 + 665 ppm Ni<sup>2+</sup> after pre-forming the SEI in LP57 (red). (c) Amounts of nickel detected after soaking a graphite electrode with SEI formed either at 25 °C (blue) or 55 °C (red) for different immersion times in nickel-contaminated electrolyte (665 ppm).

recall that this quantification does not take into account all of the dissolved nickel cations but only those deposited onto the negative electrode, thus the values are most certainly underestimated. Nevertheless, the measured quantities account for 0.98% (4.5 V) and 1.90% (4.8 V) of the LAM previously fitted for equivalent cycling times (the amount of dissolved nickel at 4.2 V was insignificant, making such comparison irrelevant). Ultimately, nickel dissolution is an integral part of the LAM process, even though electrochemical grinding and loss of electronic conductivity following particles cracking remain the main contributing factors.

As well documented in the literature, TMs dissolution can lead to “cross-talking” mechanism, bringing our attention to the interaction of TMs with the SEI at the negative electrode. First, cyclic voltammograms (CVs) were carried out using nickel-containing electrolytes (665 ppm of Ni<sup>2+</sup>, as deduced by ICP-MS measurements), revealing the presence of a reduction peak at 2.3 V vs Li<sup>+</sup>/Li associated to nickel reduction on copper surface prior to the electrolyte reduction (ethylene carbonate—EC) starting at 0.8 V vs Li<sup>+</sup>/Li (Fig. 3b). Furthermore, when forming the SEI, the intensity of the nickel reduction peak does not decrease, unlike that associated with EC reduction, showing that the SEI does not prevent nickel reduction.

Interaction between the SEI and dissolved nickel cations was further investigated by soaking pre-cycled graphite electrodes (3 cycles at C/20–D/20) in Ni-contaminated electrolyte (665 ppm in 200 μL) for different times. As shown in Fig. 3c, the amount of nickel is found to increase during the first hour of immersion. Hence, the SEI spontaneously uptakes nickel cations even at open circuit potential (OCP), in agreement with the ion-exchange mechanism previously proposed.<sup>22,31,44</sup> To understand the effect of SEI morphological properties on the ion-exchange mechanism, a thicker SEI was then formed on the surface of graphite by cycling at 55 °C.<sup>45</sup> Herein, nickel amount was found to increase to about twice the amount measured for SEI formed at 25 °C, confirming that a thicker SEI, i.e. an SEI containing more lithium cations, uptake more nickel cations from the electrolyte, alike previously discussed.<sup>22</sup> To highlight this effect, full cells were first cycled at 4.2 V to form the SEI on the surface of graphite (three C/20–D/20 cycles at 4.2 V), before to be cycled at the different cutoff voltages. Doing so, three to four times greater amount of nickel was detected at the anode (Fig. 3a, green bars). However, our soaking experiments also show that after one hour, nickel content was found to decrease for both SEIs formed at 25 or 55 °C, most certainly indicating that the SEI dissolves over

time and releases nickel cations (Fig. 3c). In definitive, ICP results confirmed that nickel is released from cycling LNO at high voltage, this phenomenon accounting for part of the positive LAM. The dissolved nickel cations subsequently incorporate into the SEI, through electrochemical reduction at ≈ 2.3 V vs Li<sup>+</sup>/Li (Fig. 3b) and following an ion exchange mechanism at open circuit potential (Fig. 3c).

Nevertheless, based on slippage and post mortem ICP-MS analysis, one cannot conclude that nickel cations released into the electrolyte is responsible for the LLI observed at the anode in Fig. 2b. The effect of nickel on the cell performance was thus separately benchmarked by adding Ni(TFSI)<sub>2</sub> salt in LP57 electrolyte. Nickel concentration was set to 665 ppm (12 mM) which was equivalent to an amount of nickel corresponding to 0.5%<sub>w/v</sub> as found at 4.8 V by ICP-MS quantifications. Graphite/LNO cells were cycled to 4.2 V using the aging/control protocol (Fig. 1a). At this low cutoff voltage, nickel dissolution can be neglected, as shown by the limited nickel amounts found in Fig. 3a, allowing to focus solely on the side effects of the added nickel. As shown in Fig. 4a, the addition of dissolved nickel strongly affects cell performances from the beginning of cycling with an average discharge capacity of 201 mAh.g<sup>-1</sup> (0th control) compared to 214 mAh.g<sup>-1</sup> measured in LP57. The concentration of added TFSI<sup>-</sup> anions in the electrolyte is too limited to disrupt the good passivation of aluminum, suggesting that dissolved Ni<sup>2+</sup> cations solely influence the initial cell chemistry, in particular the SEI formation. The gap in capacity then widens from the 13th cycle onwards for electrolytes containing dissolved nickel, with a sharp drop in capacity observed between the 2nd and the 4th control cycles, before stabilizing and returning to the same degradation rate as observed for LP57. To understand if this conclusion is unique to nickel cations, cobalt and manganese salts were also tested by adding Co(TFSI)<sub>2</sub> and Mn(TFSI)<sub>2</sub> (665 ppm) (Fig. 4a). Similar conclusions can be drawn, making this conclusion general to any TMs dissolution relevant to NMC compounds.

Slippages associated with added TMs were then analyzed. For all four electrolytes, a negative slippage is observed (blue curves), which increasingly shifts to the left over cycling and is mainly associated with LLI on graphite electrode (Fig. 4b). Positive electrode LAM also contributes to the capacity drop, but to a lesser extent, especially at low cutoff potentials. For nickel, cobalt and manganese, initial slippage values are twice that observed for LP57 (0.27 to 0.29 compared to 0.15 mAh). Furthermore, when TMs are present in the electrolyte, subsequent LLI is found to increase 1.5-

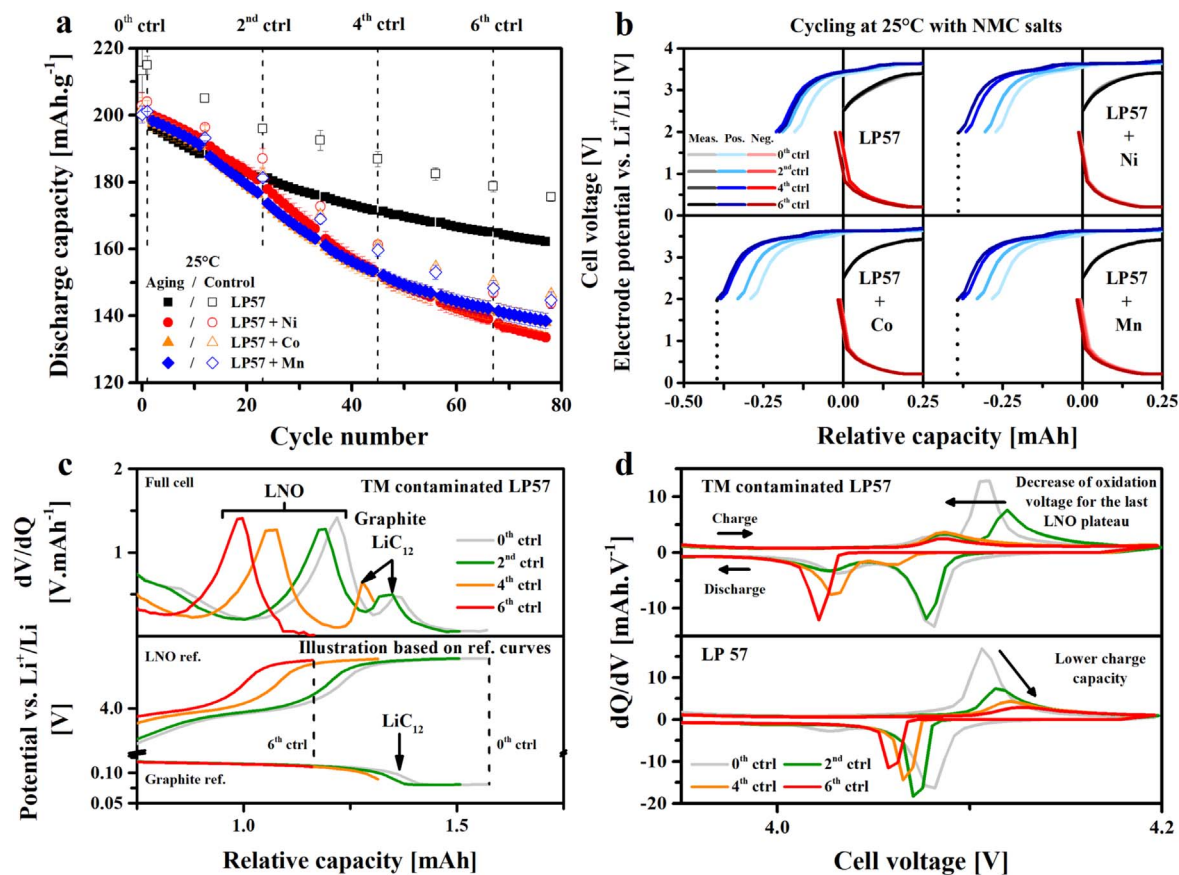


**Figure 4.** Performance degradations for TM-contaminated cells upon cycling. (a) Capacity retention measured for LP57 (black) or LP57 contaminated with 665 ppm nickel (red), cobalt (orange) or manganese (blue). Capacity is normalized by the mass of LNO active material. (b) Corresponding slippage analysis showing an increase of lithium loss inventory when TMs are added in the electrolyte. (c) Example of  $dV/dQ$  vs  $V$  curves recorded for TM-contaminated electrolyte (upper panel, Ni-containing LP57) and respective lithiation degree reached at the end of charge for both electrodes (lower panel). (d) Associated  $dQ/dV$  vs  $Q$  curves showing decrease of oxidation voltage for the last LNO plateau with Ni-contaminated electrolyte (upper panel) compared to LP57 where it is absent (lower panel).

times faster after the 0th control, more specifically between the 2nd and the 4th control, until reaching a value of about 0.4 mAh, consistent with the capacity fading observed in Fig. 4a.

The reduction reaction  $TM^{2+} + 2e^- \rightarrow TM^0$  considering an initial concentration of 665 ppm (in 30  $\mu$ L of electrolyte) would only account for ca. 0.02 mAh of the negative slippage, much less than the observed values. Therefore, TMs deposition on graphite electrodes cause an increase of LLI during the SEI formation step (initial cycles) and triggers additional lithium losses during the subsequent cycles, i.e. destabilizing the SEI during cycling. The greater LLI associated with dissolved TMs has also been discussed in previous works and was attributed to catalytic loops,<sup>26</sup> decomposition of SEI species<sup>21</sup> or SEI thickening.<sup>17</sup> Finally, the stabilization of capacity loss after the 4th control with nickel, manganese and cobalt (Fig. 4a), matches with the disappearance of the  $LiC_{12}$  feature of graphite in  $dV/dQ$  curves as a result of the greater LLI (Fig. 4c). Indeed, the LLI gradually shifts the negative electrode to a lower lithiation degree until the graphite lithiation plateau at 80 mV vs  $Li^+/Li$  is no longer reached, thus ending the charge on the upper lithiation plateau at about 110 mV vs  $Li^+/Li$  (30 mV higher). As a result, the voltage for the last LNO intercalation plateau progressively decreases to 4.08 V during charge in full cell with contaminated electrolytes (Fig. 4d), compared to 4.11 V with LP57. Indeed, while rising of the cell impedance gradually hinders the last oxidation plateau of LNO in LP57 as observed in the  $dQ/dV$  analysis (lower panel, Fig. 4d), the lower reaction voltage reached when adding TMs allows to access greater state of charge for LNO before reaching the 4.2 V cutoff voltage. Therefore, the apparent stabilization of the capacity

retention over cycling originates from the greater delithiation stage reached by LNO in charge. Nevertheless, this phenomenon cannot be solely associated with a raise of negative potential and likely implies other mechanisms such as the gradual stabilization of the SEI. Hence, Dose et al. showed similar aging behavior for graphite/NMC811 cells which graphite anode experienced a jump in potential upon LLI.<sup>46</sup> Subsequent raise of NMC811 potential at the end of charge triggers greater structural damages which, ultimately, accelerate the capacity losses. Whilst similar degradations are eventually expected for LNO, re-accessing the LNO plateau at 4.2 V corresponding to 40  $mAh.g^{-1}$  initially slows down the capacity fading. However, over prolonged cycling, deleterious  $H2 \rightarrow H3$  phase transition at 4.2 V would prematurely fatigue bulk LNO and precipitate the capacity fading. Thus, despite a similar origin rooted in a change in staging at the graphite electrode associated with copious LLI, cell performance are directly influenced by the nature of the positive electrode material and its working potential. However, the origin for the increase LLI for electrolytes contaminated with TMs is not elucidated at that stage.

To understand if the incorporation of TMs into the SEI induces rollover failure associated with lithium plating on the graphite surface, as previously proposed,<sup>29,30,47</sup> a dedicated protocol was then used. Indeed, although lithium plating may induce LLI as observed in this study, a clear demonstration of the causal relationship between TMs and plating remains complex as these phenomena depend on parameters such as voltage, current and temperature.<sup>48–52</sup> In addition, detection of plating phenomenon by post mortem characterizations is not trivial as metallic lithium can be re-intercalated into graphite

during relaxation time, masking its presence.<sup>49,51–54</sup> Therefore, rather than using post mortem characterization techniques, we took inspiration from recent works in which activation energies ( $A_E$ ) for cell capacity loss<sup>55</sup> were extracted from temperature-dependent measurements to distinguish between two degradation regimes: one dominated by the SEI growth and the second by lithium plating. However, no standardized protocol currently exists for such study, especially performed using laboratory scale cells (coin cells). Hence, previous reports used commercial cells and defined degradation rate by the time<sup>56</sup> or cycle number<sup>55</sup> necessary to reach 80% state of health (i.e. 80% of the initial experimental capacity). However, substantial information are lost by averaging degradation rates over such a prolonged period of time, which may potentially hide some modification of the degradation regime over cycling. Herein, we thus assess degradation rates between a fixed number of cycles, i.e. from control number  $N$  to  $N + 1$  or  $N + 2$ , and define the rate as the capacity loss (mAh) normalized by time (h), active material mass (g) and surface ( $\text{cm}^2$ ) to ensure comparison with future studies carried out in similar coin cells configuration.

Graphite/LNO cells were first cycled at low C-rate ( $C/2$ ) to favor SEI-dominated degradations, and the results then compared with those obtained at high C-rate (3 C) for which plating is favored (Fig. 5a). For LP57, plotting the degradation rates measured at 3 C (orange dots) as a function of reciprocal temperature ranging from 15 °C to 55 °C (i.e. Arrhenius plot), two slopes are obtained, indicating two distinct degradation mechanisms. At high temperatures ( $T > 35$  °C), the degradation is associated with interfacial degradations, including SEI growth (Activation energy,  $A_E > 0$ ), while at low temperature ( $T < 35$  °C), lithium plating dominates the degradation rates ( $A_E < 0$ , positive slope). In other words, with increasing temperature, chemical reactions including those forming the SEI are accelerated and consume more lithium, while at low temperatures they become sluggish which, combined with the slow intercalation reactions, favored lithium plating on graphite surface. For low C-rate ( $C/2$ , grey squares), degradations follow a SEI growth regime ( $A_E > 0$ ) over the whole temperature range, indicating that no lithium plating occurs, or in very limited fashion. This observation remains valid through cycling, i.e. between control 0 and 1 ( $C0-C1$ ), control 1 and 2 ( $C1-C2$ ) or control 2–3 ( $C2-C3$ ) (Figs. 5b and 5c). In addition, the decreased degradation rates observed over cycling is consistent with a stabilization of the SEI, as previously observed by a reduction of LLI (Fig. 2b). Ultimately, C-rate is decisive in favoring plating or not, providing an opportunity to study the influence of dissolved TMs on aging mechanisms.

To study the influence of TMs in plating conditions, tests at 3 C with LP57 were first performed as a benchmark (Fig. 6a), revealing a switch from positive to negative for activation energies at 35 °C. Lithium plating is thus favored below 35 °C, corroborating previous study carried out by Yang and co.<sup>55</sup> where plating started at 40 °C at 3 C (with a balancing N/P = 1.2). Thereafter, cells were cycled with electrolytes containing dissolved TMs and degradation rates were found to show a single slope ( $A_E > 0$ ), unlike for bare LP57 (Fig. 6a). This observation indicates that the SEI growth regime remains dominant for nickel and manganese contaminated electrolytes across the whole temperature range, thus hiding any effect associated with lithium dendrite formation even at large C-rate such as 3 C. This result is not associated with a raise of graphite potential at the end of charge, as previously discussed in Fig. 4c, which may have masked plating.<sup>48</sup> Finally, these conclusions are specific to the experimental conditions, and plating may become the dominant degradation regime at low temperature for contaminated electrolytes when further decreasing the balancing.

## Conclusions

In this work, a set of electrochemical protocols was used to study degradations associated with TM dissolution in graphite/LNO cells. We first confirmed via ICP-MS quantifications that while dissolved nickel accounts for less than 1% of the total amount of nickel in the active material, TM cations are incorporated in the SEI either via electrochemical or spontaneous absorption pathways. The analysis of capacity slippage from  $dV/dQ$  curves then revealed that all TMs (nickel, cobalt and manganese) disrupt the cell operation in a similar manner, i.e. through greater LLI in particular during the initial cycles. In other words, TMs incorporated in the SEI act as damaging agents which favor parasitic reactions, and thus lithium losses. Interestingly, we showed that capacity losses induced by TMs tend to slow down after 50 cycles, which matches with a raise of graphite potential charge end point. This observation does not question the damaging effect of TMs but rather highlight a specificity of the graphite/LNO system, where a raise of negative potential charge end point slows down, at least during few cycles, the loss of capacity during the high voltage LNO plateau. However, over prolonged cycling, LNO fatigue at high potential will anyway precipitate the death of the cell. Hence, we demonstrate that special care must be exercised when assigning capacity loss over cycling to a given effect, and that proper electrochemical protocols are required. We then investigated the origins for LLI observed with TMs using a dedicated protocol based on temperature aging measurements.

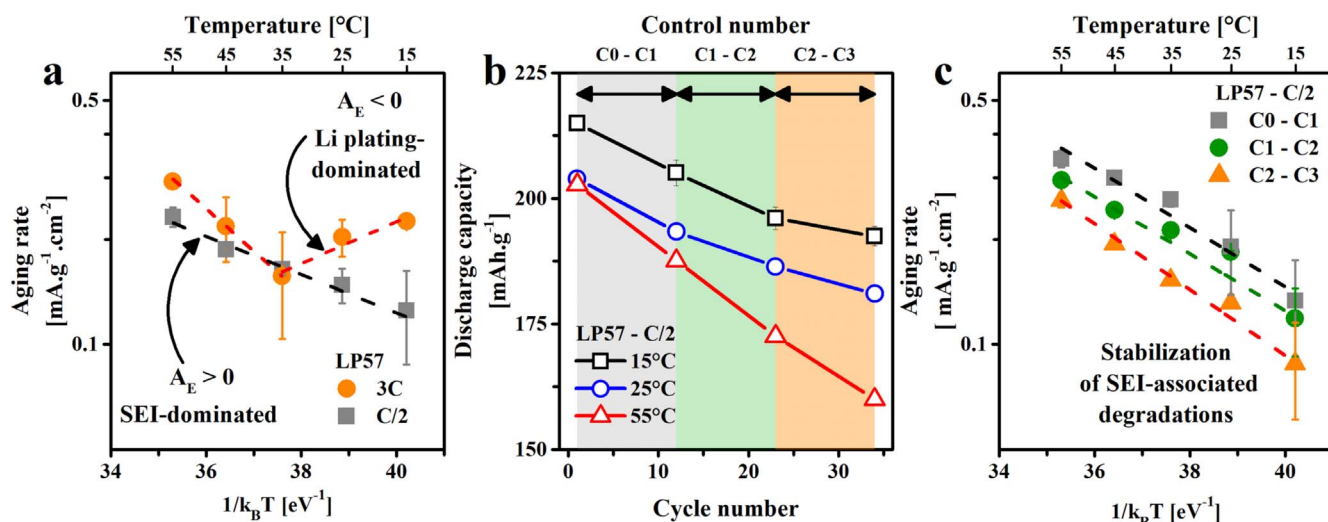


**Figure 5.** Effect of current density and cycle number on degradations rates. (a) Arrhenius plot of the degradation rates recorded for graphite/LNO cells at 3 C (orange) or  $C/2$  (grey) current between control 0 and 2. (b) Discharge capacities recorded during the first control cycles in LP57 at  $C/2$  at different temperatures. Lines are guide to the eyes. (c) Arrhenius plots for the degradation rates recorded between 0th and 1st control (grey), 1st and 2nd (green) and 2nd and 3rd (orange).

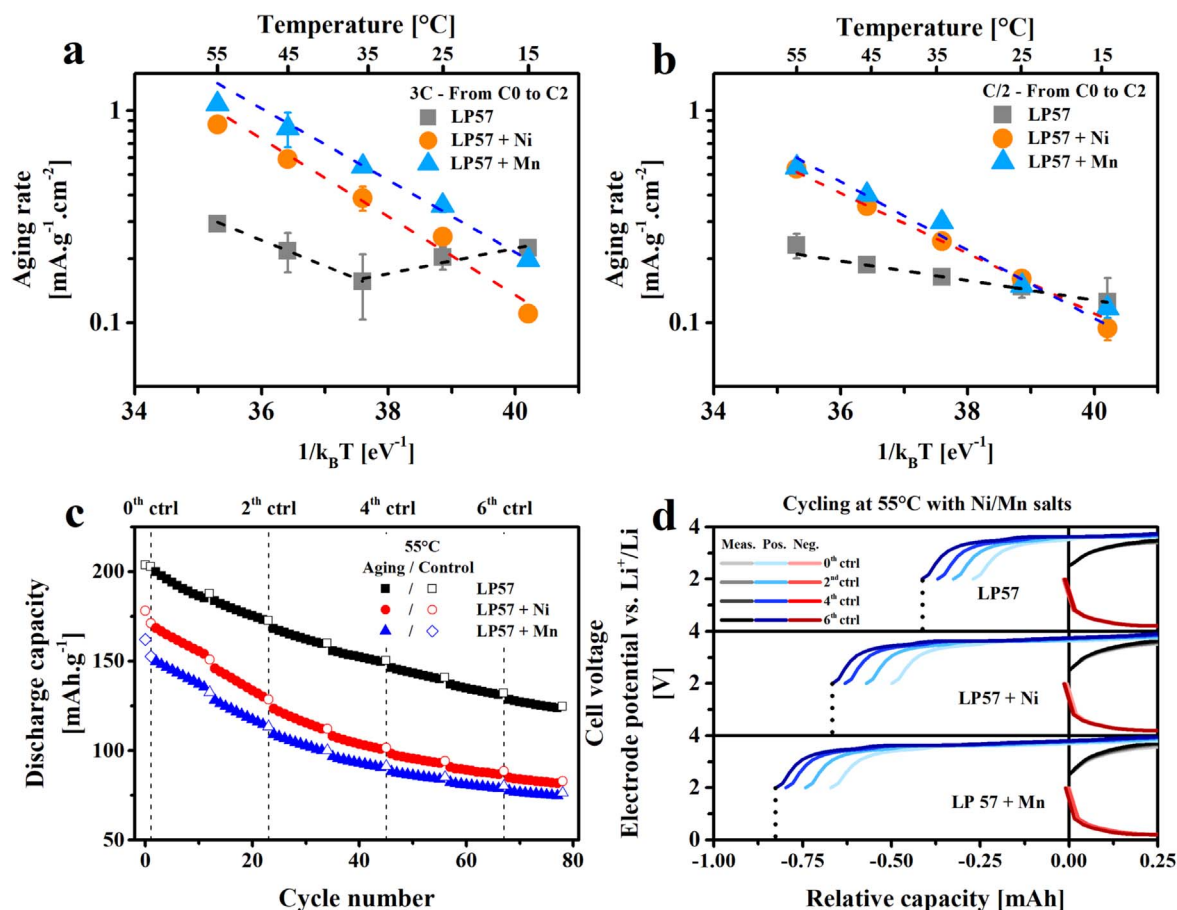


**Figure 6.** Effect of dissolved TMs on lithium plating and SEI growth. Arrhenius plots recorded for nickel- (orange) and manganese-containing (blue) LP57 electrolytes compared to LP57 (grey) at 3 C (a) and at C/2 (b). (c) Capacity retention for graphite/LNO cells cycled at 55 °C in LP57 (black), LP57 + 665 ppm Ni<sup>2+</sup> (red) and LP57 + 665 ppm Mn<sup>2+</sup> (blue). Capacities are normalized by LNO active material weight. (d) Associated slippage analysis from 0th to 6th control cycle showing an increase of LLI at elevated temperature with nickel or manganese.

We found that TM deposition at the anode favors degradation mechanisms associated with SEI growth, this effect being predominant when compared to any effect related to lithium plating, unlike previously proposed in the literature. Finally, we demonstrate an activation of TM reactivity at elevated temperatures with massive LLI.

Hence, we believe that proper electrochemical methodology can be designed beyond simple evaluation of the cell performance to assess complex interfacial effects and probe the origin for cell degradation in a non-invasive manner. All of the protocols described in this work can be fully transposed to other LIB chemistries, in particular technology-relevant ones using materials such as NMC811 or Si-graphite also suffering from drastic interfacial instabilities, as well as more complex electrolytes incorporating additives<sup>57,58</sup> or even to super-concentrated electrolytes that were previously proposed to limit TMs solubility.<sup>59–61</sup>

### Acknowledgments

This project has received funding from the European Union's Horizon 2020 research and innovation program under grant agreement No. 957189. The authors thank F. Rabuel (LRCS, France) for manufacturing LNO and graphite electrodes for the study. The authors thank the Department of Physics and Atmospheric Science, Dalhousie University for providing dV/dQ fitting freeware (VAWQuum v1.2).

### ORCID

Valentin Meunier <https://orcid.org/0000-0002-8042-4182>  
Alexis Grimaud <https://orcid.org/0000-0002-9966-205X>

### References

- O. Gröger, H. A. Gasteiger, and J.-P. Suchsland, *J. Electrochem. Soc.*, **162**, A2605 (2015).
- J. Amici et al., *Adv. Energy Mater.*, **12**, 2102785 (2022).
- A. Manthiram, *Nat. Commun.*, **11**, 1 (2020).
- W. Li, E. M. Erickson, and A. Manthiram, *Nat. Energy*, **5**, 26 (2020).
- S. Dühnen, J. Betz, M. Kolek, R. Schmuch, M. Winter, and T. Placke, *Small Methods*, **4** (2020).
- J. Li, L. E. Downie, L. Ma, W. Qiu, and J. R. Dahn, *J. Electrochem. Soc.*, **162**, A1401 (2015).
- K. J. Park, J. Y. Hwang, H. H. Ryu, F. Maglia, S. J. Kim, P. Lamp, C. S. Yoon, and Y. K. Sun, *ACS Energy Lett.*, **4**, 1394 (2019).
- H. H. Ryu, G. T. Park, C. S. Yoon, and Y. K. Sun, *Small*, **14**, 1 (2018).
- A. O. Kondrakov, A. Schmidt, J. Xu, H. Geßwein, R. Mönig, P. Hartmann, H. Sommer, T. Brezesinski, and J. Janek, *J. Phys. Chem. C*, **121**, 3286 (2017).
- F. Lin, I. M. Markus, D. Nordlund, T. C. Weng, M. D. Asta, H. L. Xin, and M. M. Doeff, *Nat. Commun.*, **5**, 3529 (2014).
- J. Li, H. Liu, J. Xia, A. R. Cameron, M. Nie, G. A. Botton, and J. R. Dahn, *J. Electrochem. Soc.*, **164**, A655 (2017).
- D. P. Abraham, R. D. Twisten, M. Balasubramanian, I. Petrov, and J. McBreen, *Electrochemistry Communications*, **4**, 620 (2002).
- Y. Zhang et al., *Energy Environ. Sci.*, **13**, 183 (2020).
- L. Giordano, P. Karayalali, Y. Yu, Y. Katayama, F. Maglia, S. Lux, and Y. Shao-Horn, *J. Phys. Chem. Lett.*, **8**, 3881 (2017).
- B. Stiaszny, J. C. Ziegler, E. E. Krauß, M. Zhang, J. P. Schmidt, and E. Ivers-Tiffée, *J. Power Sources*, **258**, 61 (2014).
- D. R. Gallus, R. Schmitz, R. Wagner, B. Hoffmann, S. Nowak, I. Cekic-Laskovic, R. W. Schmitz, and M. Winter, *Electrochim. Acta*, **134**, 393 (2014).
- J. A. Gilbert, I. A. Shkrob, and D. P. Abraham, *J. Electrochem. Soc.*, **164**, A389 (2017).
- I. H. Cho, S. S. Kim, S. C. Shin, and N. S. Choi, *Electrochem. Solid-State Lett.*, **13**, 168 (2010).
- L. M. Thompson, W. Stone, A. Eldesoky, N. K. Smith, C. R. M. McFarlane, J. S. Kim, M. B. Johnson, R. Petibon, and J. R. Dahn, *J. Electrochem. Soc.*, **165**, A2732 (2018).

20. S. Komaba, N. Kumagai, and Y. Kataoka, *Electrochim. Acta*, **47**, 1229 (2002).
21. S. Solchenbach, G. Hong, A. T. S. Freiberg, R. Jung, and H. A. Gasteiger, *J. Electrochem. Soc.*, **165**, A3304 (2018).
22. C. Zhan, X. Qiu, J. Lu, and K. Amine, *Adv. Mater. Interfaces*, **3**, 1 (2016).
23. C. Delacourt, A. Kwong, X. Liu, R. Qiao, W. L. Yang, P. Lu, S. J. Harris, and V. Srinivasan, *J. Electrochem. Soc.*, **160**, A1099 (2013).
24. T. Joshi, K. Eom, G. Yushin, and T. F. Fuller, *J. Electrochem. Soc.*, **161**, A1915 (2014).
25. R. Jung, F. Linsenmann, R. Thomas, J. Wandt, S. Solchenbach, F. Maglia, C. Stinner, M. Tromp, and H. A. Gasteiger, *J. Electrochem. Soc.*, **166**, A378 (2019).
26. K. Leung, *Chem. Mater.*, **29**, 2550 (2017).
27. Y. Li, M. Bettge, B. Polzin, Y. Zhu, M. Balasubramanian, and D. P. Abraham, *J. Electrochem. Soc.*, **160**, A3006 (2013).
28. S. Klein, P. Bärnmann, T. Beuse, K. Borzutzki, J. E. Frerichs, J. Kasnatscheew, M. Winter, and T. Placke, *ChemSusChem*, **14**, 595 (2021).
29. S. Klein, S. Röser, P. Bärnmann, K. Borzutzki, B. Heidrich, M. Börner, M. Winter, T. Placke, and J. Kasnatscheew, *Adv. Energy Mater.*, **11**, 2003738 (2021).
30. S. Klein, P. Bärnmann, L. Stolz, K. Borzutzki, J. P. Schmiegel, M. Börner, M. Winter, T. Placke, and J. Kasnatscheew, *ACS Appl. Mater. Interfaces*, **13**, 57241 (2021).
31. C. Zhan, J. Lu, A. Jeremy Kropf, T. Wu, A. N. Jansen, Y. K. Sun, X. Qiu, and K. Amine, *Nat. Commun.*, **4**, 1 (2013).
32. H. Shin, J. Park, A. M. Sastry, and W. Lu, *J. Power Sources*, **284**, 416 (2015).
33. S. Fang, D. Jackson, M. L. Dreibeilbis, T. F. Kuech, and R. J. Hamers, *J. Power Sources*, **373**, 184 (2018).
34. J. Wandt, A. Freiberg, R. Thomas, Y. Gorlin, A. Siebel, R. Jung, H. A. Gasteiger, and M. Tromp, *J. Mater. Chem. A*, **4**, 18300 (2016).
35. S. R. Gowda, K. G. Gallagher, J. R. Croy, M. Bettge, M. M. Thackeray, and M. Balasubramanian, *Phys. Chem. Chem. Phys.*, **16**, 6898 (2014).
36. I. Bloom, A. N. Jansen, D. P. Abraham, J. Knuth, S. A. Jones, V. S. Battaglia, and G. L. Henriksen, *J. Power Sources*, **139**, 295 (2005).
37. I. Bloom, J. Christophersen, and K. Gering, *J. Power Sources*, **139**, 304 (2005).
38. I. Bloom, J. P. Christophersen, D. P. Abraham, and K. L. Gering, *J. Power Sources*, **157**, 537 (2006).
39. I. Bloom, L. K. Walker, J. K. Basco, D. P. Abraham, J. P. Christophersen, and C. D. Ho, *J. Power Sources*, **195**, 877 (2010).
40. H. M. Dahn, A. J. Smith, J. C. Burns, D. A. Stevens, and J. R. Dahn, *J. Electrochem. Soc.*, **159**, A1405 (2012).
41. A. J. Smith, H. M. Dahn, J. C. Burns, and J. R. Dahn, *J. Electrochem. Soc.*, **159**, A705 (2012).
42. A. J. Smith, J. C. Burns, D. Xiong, and J. R. Dahn, *J. Electrochem. Soc.*, **158**, A1136 (2011).
43. F. Wu et al., *Nano Energy*, **59**, 50 (2019).
44. C. Zhan, T. Wu, J. Lu, and K. Amine, *Energy Environ. Sci.*, **11**, 243.
45. Z. I. Minoru, H. Tomiyasu, A. Tasaka, S. K. Jeong, Y. Iriyama, T. Abe, and Z. Ogumi, *Electrochemistry*, **12**, 71 (2003).
46. W. M. Dose, C. Xu, C. P. Grey, and M. F. L. De Volder, *Cell Reports Physical Science*, **1**, 100253 (2020).
47. S. Klein, P. Harte, S. van Wickeren, K. Borzutzki, S. Röser, P. Bärnmann, S. Nowak, M. Winter, T. Placke, and J. Kasnatscheew, *Cell Reports Physical Science*, **2**, 100521 (2021).
48. M. Petzl, M. Kasper, and M. A. Danzer, *J. Power Sources*, **275**, 799 (2015).
49. U. R. Koleti, T. Q. Dinh, and J. Marco, *J. Power Sources*, **451**, 227798 (2020).
50. J. C. Burns, D. A. Stevens, and J. R. Dahn, *J. Electrochem. Soc.*, **162**, A959 (2015).
51. C. Von Lüders, V. Zinth, S. V. Erhard, P. J. Osswald, M. Hofmann, R. Gilles, and A. Jossen, *J. Power Sources*, **342**, 17 (2017).
52. X. G. Yang, S. Ge, T. Liu, Y. Leng, and C. Y. Wang, *J. Power Sources*, **395**, 251 (2018).
53. V. Zinth, C. Von Lüders, M. Hofmann, J. Hattendorff, I. Buchberger, S. Erhard, J. Rebelo-Kornmeier, A. Jossen, and R. Gilles, *J. Power Sources*, **271**, 152 (2014).
54. T. Waldmann, B. I. Hogg, and M. Wohlfahrt-Mehrens, *J. Power Sources*, **384**, 107 (2018).
55. X. G. Yang and C. Y. Wang, *J. Power Sources*, **402**, 489 (2018).
56. T. Waldmann, M. Wilka, M. Kasper, M. Fleischhammer, and M. Wohlfahrt-Mehrens, *J. Power Sources*, **262**, 129 (2014).
57. H. Liu, A. J. Naylor, A. S. Menon, W. R. Brant, K. Edström, and R. Younesi, *Adv. Mater. Interfaces*, **7**, 2000277 (2020).
58. Y. Zhu, Y. Li, M. Bettge, and D. P. Abraham, *J. Electrochem. Soc.*, **159**, A2109 (2012).
59. N. Dubouis et al., *Nat. Mater.*, **20**, 1545 (2021).
60. Y. Yamada, J. Wang, S. Ko, E. Watanabe, and A. Yamada, *Nat. Energy*, **4**, 269 (2019).
61. W. Liu, J. Li, W. Li, H. Xu, C. Zhang, and X. Qiu, *Nat. Commun.*, **11**, 3629 (2020).